Check for updates

A micelle-templated nanoparticle contrast agent enables dynamic microscale X-ray computed tomography imaging of the soil aqueous phase

Shuchen Wang,[a] Anna P. Constantinou,[a] Guanglei Zhang,[b] Yihuai Zhang,†[b] Mohammad Javad Shojaei,[b] Bo Zhou, [ID][a] Davey L. Jones,[c] Tiina Roose,[d] Martin J. Blunt,[b] Theoni K. Georgiou [ID][a] and Iain E. Dunlop [ID] *[a]

The need to develop alternative agricultures that preserve soil health with reduced contribution to climate change has led to growing interest in soil's microscale structure and dynamics. Microscale X-ray computed tomography (μX-CT) can image soil mineral particles at high-resolution but does not readily distinguish low-density aqueous and organic phases, nor image fluid and nutrient transport. Here we have developed polymer-templated gold nanoparticles as a contrast agent to label the aqueous phase in soil, selecting gold for low toxicity. Nanoparticles are created by templated synthesis inside block copolymer micelles with a stabilizing corona: poly(2-(dimethylamino)ethyl methacrylate)-*block*-poly[poly(ethylene glycol)methyl ether methacrylate]. These gold-polymer nanoparticles (gold core diameter 12 nm; overall hydrodynamic diameter 44 nm) are generated at high concentrations and in large volumes for soil imaging. They show exceptional colloidal stability (to ≥1.5 M ionic strength), and are stable in the soil microenvironment, with no adsorption to mineral particles. *In situ* μX-CT imaging distinguished nanoparticle-labelled soil aqueous phase from unlabelled aqueous phase, at ~5 mg ml^{-1} Au. Dynamic imaging determined the nanoparticle bulk diffusion constant in soil to be $1.1 \pm 0.3 \times 10^{-10}$ m^2 s^{-1}, much slower than typical single-ion transport in soil. We propose these nanoparticles as an effective contrast agent for flow and transport imaging in living soil.

Introduction

Soil plays a key role in sustaining both human societies and terrestrial ecosystems. As a biogeochemical engine of the Earth's life support system, soil fulfils many crucial functions.[1,2] Soil anchors plant roots and serves as a reservoir of essential nutrients. Furthermore, it acts as a natural filtration system for rainwater, safeguarding underground water sources by buffering against waste and pollutants.[2,3] Besides these practical functions, soil is the largest terrestrial repository of organic carbon,[4] storing more than three times the amount of organic carbon found in vegetation and approxi-

mately twice as much as the atmosphere.[5] This has contributed to a recent upsurge in interest in agricultural management strategies that aim to improve carbon storage as well as preserving or improving soil resources for future generations. These include methods such as reduced tillage and regenerative agriculture, as well the adoption of new agrochemical approaches that aim to work with rather than against natural soil biology and structure.[6–8]

All the functions of soil in ecology and agriculture are founded on its inherently complex 3D structure and dynamics. The combination of mineral grains of various sizes, pores fulfilled with water and air, together with organic materials, and living plant roots and microbiome makes soil "the most complex biomaterial on the planet".[9] 3D dynamic processes include the flow and transport of water, gases, nutrients and pathogens, as well as the growth of roots, fungi and microbial colonies.[10] Understanding soil as a functional biophysical system therefore requires the ability to image and characterize these 3D structures and processes, at high spatial and temporal resolution.

Over the past few decades, many studies have investigated soil functioning using a wide range of 3D imaging techniques.

[a]*Department of Materials, Faculty of Engineering, Imperial College London, Exhibition Road, London SW7 2AZ, UK. E-mail: i.dunlop@imperial.ac.uk*
[b]*Department of Earth Sciences and Engineering, Faculty of Engineering, Imperial College London, Exhibition Road, London SW7 2AZ, UK*
[c]*School of Environmental and Natural Sciences, Bangor University, Bangor, Gwynedd, LL57 2UW, UK*
[d]*School of Engineering, Faculty of Engineering and Physical Sciences, University of Southampton, University Road, Southampton, Hampshire SO17 1BJ, UK*
†Current address: James Watt School of Engineering, University of Glasgow, G12 8QQ, United Kingdom.

For example, thermal neutron tomography has been used to study the distribution of water within soil,[11,12] while magnetic resonance imaging (MRI) has revealed root structures and water.[13,14] These techniques have revealed valuable insights at the larger spatial scale (e.g. resolutions of ∼80 μm for neutron tomography,[11] and 600 μm for MRI[14]). However many soil processes operate at lengthscales much smaller than this (∼1–10 μm) reflecting the multiscale nature of soil pore structure. Equally some key biological structures such as fungal hyphae are also of order 20 μm or less. Hence to obtain a genuinely microscale understanding of soil structure and dynamics, a higher resolution technique is needed, and the leading technique in this context is microscale X-ray computed tomography (μX-CT), with resolution down to ∼1 μm on typical setups.[15,16]

μX-CT generates a contrast based on the electron density of soil components, which means it is unaffected by the magnetic properties of soil components in contrast to MRI.[17] μX-CT provides excellent imaging of the mineral phases of soil, e.g. aluminosilicates, since there is a strong contrast between these electron-dense phases and the lower-density phases: water and dead organic matter, and living materials. This has enabled application of μX-CT to characterise soil properties such as pore-space geometry and fractures, investigation of pore network structures, layer detection and volumetric water content analysis.[18–21] However, there is a significant challenge to distinguish between organic materials and the water phase, due to their similarities in X-ray attenuation coefficients.[22] This is critical to transport measurements since organic matter is extremely prevalent in soil, so images of pore structure based on mineral phases alone are insufficient to fully determine the paths that water can follow. Rather there is a need to directly and dynamically visualize aqueous-phase flow and transport. Similarly, while segmentation of organic phases becomes easier for large extended structures such as some plant root systems, using e.g. advanced computational workflows or low-energy X-rays,[22–25] segmentation at shorter length-scales remains extremely challenging.

Similar issues are encountered in biomedical X-CT imaging, where there is a need to distinguish different fluids and soft tissues from one another, despite their similar electron densities. In this case, a common solution is to use contrast agents to label areas of interest, where contrast agents are solutions or particles that contain elements with high attenuation coefficients such as iodine, barium or lanthanides or other heavy metals.[26] This concept has equally been applied to label liquid phases in investigations of flow through porous rock for applications in hydrocarbon recovery and carbon dioxide storage, typically using iodinated contrast agents.[27–29] A number of studies have applied these contrast agents to soil imaging, visualizing both flows and plant root systems.[30–34] However, it is notable that their phytotoxicity can cause dehydration, distortion and damage to plant tissues.[31–34] Other contrast agents that have been applied in soil include osmium tetroxide, which exhibits limited penetration ability, along with very high toxicity, as well as bismuth tartrate, which

requires a prolonged incubation period that makes it unsuitable for many applications.[30] These pioneering investigations have shown the value that contrast agents can bring in soil science, underlining the potential benefits of an agent that is non-toxic and can be used at large scale in imaging biologically active soil.

In biomedical imaging many labs have sought to develop gold nanoparticles that are functionalized with biomolecules, as X-CT contrast agents that are targeted specifically to label cancerous tissue. Despite success in preclinical studies, these have not yet been translated into clinical practice.[35] In the different context of soil science, however, their highly tailorable and non-toxic nature makes them an ideal candidate as a contrast agent. As-synthesized gold nanoparticles made by standard methods such as citrate reduction[36] cannot, however, be used for this application. This is because their colloidal stability relies on electrical charge, meaning that they will flocculate (stick together) under the electrolyte conditions present in soil.[37] Equally, they will non-specifically adhere to the solid surfaces of soil minerals. In a bionanoscience context, the analogous issues are typically addressed by a multi-step process whereby gold nanoparticles are first synthesized using small-molecule surfactants, and then these surfactants are displaced from the nanoparticle surface by the application of thiol-functionalized poly(ethylene glycol) (PEG). The PEG forms an antifouling corona that protects the nanoparticle from flocculation and/or surface interactions, and its biocompatiblility ensures the non-toxic nature of the resulting nanostructure. In a recent preliminary study, we demonstrated that gold nanoparticles created using this standard method are stable in soil and can be used as a flow tracer.[37] This was achieved by functionalizing commercially available citrate-reduced gold nanoparticles with a heterobifunctional PEG reagent (α-methoxy-ω-mercapto PEG (CH$_3$O-PEG-SH)), which must be done under dilute solution conditions, and then intensively concentrating to generate the high concentrations required for soil X-CT imaging. Hence while technically successful, this method generates a reagent cost of the order of thousands of dollars per soil sample imaged, precluding practical application in environmental sciences.

Here, we have developed a new gold nanoparticle contrast agent, based on an approach of polymer-micelle-templated synthesis,[38–41] leading to a stable and effective contrast system that is also scalable. In this approach, block copolymer spherical micelles are first assembled as nanoreactors. The micelles combine a hydrophobic amine-rich core with a hydrophilic corona. Upon addition of a precursor solution that contains gold(III) chloride (HAuCl$_4^-$) ions, these ions concentrate at the micelle cores due to complexation by the amine groups. The amines simultaneously act as reducing agents, converting gold (III) to metallic gold(0) and leading to the formation of a gold nanoparticle in the core of the micelle.

We here implemented this concept using a diblock copolymer: poly(2-(dimethylamino)ethyl methacrylate)-block-poly [poly(ethylene glycol)methyl ether methacrylate], poly (DEAEMA-b-PEGMA), where the amine-rich polyDEAEMA

© 2025 The Author(s). Published by the Royal Society of Chemistry

RSC Appl. Polym., 2025, 3, 1596–1612 | 1597

becomes hydrophobic to form a micelle core at c pH7.[38,39] The polyPEGMA block forms a bottle-brush-like structure with many short (4.5 ethylene glycol units) PEG chains grafted along the backbone, giving a high PEG density that is highly stabilizing. Because nanoparticles are produced already stabilized within these micelle structures, synthesis can be carried out at very high concentrations without loss of stability. Finally, the diblock copolymers are synthesized using group transfer polymerization (GTP). GTP is a highly scalable living anionic polymerization process that produces controlled architecture polymers with narrow molar mass distributions comparable to those generated by other anionic polymerization methods, or by controlled/living radical polymerizations such as ATRP [atom transfer radical polymerization] and RAFT [reversible addition fragmentation chain transfer].[42] However, compared to other polymerization methods, it is an industrially developed technique that offers key advantages in terms of ease of production, cost and potential for scalability.[43–46] GTP can be performed in large batches, at room temperature, and at higher concentrations, in a remarkably rapid (~15 min for the polymers in the present study) one-step process without intermediate purification steps.

In this study we created and tested in application a nanoparticle contrast agent using micelle-templating with diblock copolymers synthesized by GTP. We will show below that this approach generates a stable, high-performance, and practicable option for soil X-CT imaging.

Results

Diblock copolymer synthesis

Amphiphilic copolymers were synthesized based on 2-(diethylamino)ethyl methacrylate (DEAEMA) and poly(ethylene glycol) methyl ether methacrylate (average molar mass = 300 g mol^{-1}, average number of ethylene glycol units = 4.5) (PEGMA). As stated, DEAEMA was chosen as the hydrophobic monomer containing amine groups which form the micelle core, while PEGMA was chosen as the hydrophilic monomer to generate a bottle-brush anti-fouling corona around the micelle core.‡ Fig. 1(a) shows a schematic representation of the polymer, and how it self-assembles into micelles to form nano-reactors for the generation of gold nanoparticles. Synthesis was carried out using GTP, as described in detail in Materials and Methods. PEGMA$_{17}$-b-DEAEMA$_{27}$ was the target composition, giving a target molar mass 10 000 g mol^{-1}. This target composition is selected with a high DEAEMA to PEGMA ratio, aiming for a high gold loading per micelle and so ultimately a strong X-ray contrast from the nanoparticle system. Successful polymerisation was confirmed by proton nuclear magnetic resonance spectroscopy (^{1}H NMR) (Fig. 1b) and gas permeation chromatography (GPC) (Fig. 1c). Experimentally-measured weight

percentages of PEGMA and DEAEMA (Table 1) were calculated by the integral ratio of PEGMA and DEAEMA signals in ^{1}H-NMR using non-overlapping peaks (signals from the CH$_2$ ethyl group next to N and closer to ester at 2.6 ppm and the methoxy peak at 3.35 ppm, respectively). The GPC chromatogram (Fig. 1c) has no shoulder or monomer peak, which indicates all monomer has polymerised and that all polymer chains grow to produce the diblock copolymer. The diblock copolymer and its linear precursor are relatively monodisperse, with $Đ$ values all lower or equal to 1.2, and the block M_n (number average molar mass) values close to those targeted (Table 1). The pK_a value of the copolymer was determined to be 7.2 by titration (using a 1 w/w% aqueous solution of the copolymer), arising from the tertiary amine groups in the DEAEMA block. Finally, the cloud-point was measured by UV-visible spectroscopy as 56 °C (also at 1% w/w), consistent with previous studies.[38]
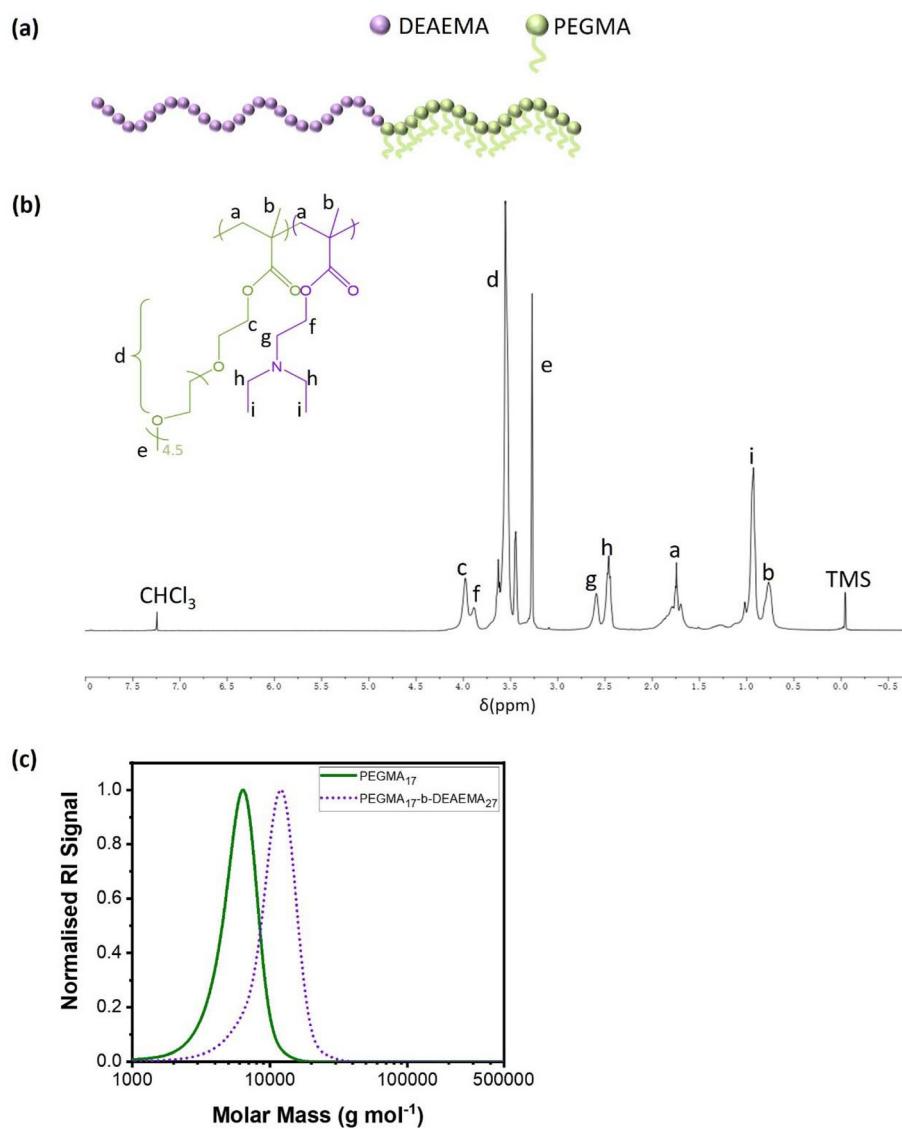
Micelle-templated gold nanoparticles: synthesis and characterization

The fabrication process of gold nanoparticles (AuNP) is illustrated schematically in Fig. 2(a). The optimal pH for formation of AuNP inside the polymer micelles will be close to the amine's pK_a.[38] This is probably because at low pH ≪ pK_a the amine group lone electron pairs will almost all be protonated and hence unavailable to complex the gold(III) chloride ions, whereas at high pH ≫ pK_a the micelle core will be very tightly bound due to the hydrophobicity, preventing the gold(III) chloride ions from infiltrating.

Nanoparticles were synthesised by separately adjusting aqueous solutions of copolymer and gold(III) chloride to pH7.5, before mixing. Concentrations were selected to give a final polymer concentration of 1% w/w, with the molar ratio of HAuCl$_4$ to DEAEMA varied as follows: 0.1, 0.3, 0.5 and 0.7, with the concept that the number of amine groups that can be successfully complexed is probably <100%. The reaction mixture was incubated at room temperature for 48 h with shaking, during which time gold nanoparticle formation was visible *via* a colour change to intense wine-red. This was confirmed by ultraviolet-visible spectroscopy (UV-vis) showing a single peak at 520 nm (Fig. 2b), increasing over time (Fig. 2c). The hydrodynamic size of the gold nanoparticles, including the polymer corona, was determined by dynamic light scattering (DLS), and was found to be in the vicinity of 40 nm for all levels of gold-loading. We also note the presence of some free polymer molecules (Fig. S3). In parallel, the zeta potential was measured (Table 2). The expectation was that there must be some positive charge in the DEAEMA-rich micelle core, due to the secondary amine groups. The impact of this charge on the zeta potential, which reflects the effective surface charge experienced at the outer hydrodynamic edge, will however reduce substantially due to the PEGMA corona, which creates a significant distance between the amine charges and the hydrodynamic edge. Measurements indeed showed a positive charge, and this increased significantly with the size of the gold particle, which may be attributed to the larger gold core displacing the amine groups closer to the outer edge of the

---

‡Given its short length, the PEGMA macromonomer should strictly be termed OEGMA, but we call it PEGMA for clarity given the well-known status of PEG in biomaterials science.

Fig. 1 (a) Schematic representation of the polymer investigated in this study. The PEGMA and DEAEMA units are shown in green and purple spheres, respectively. (b) The ^{1}H NMR spectrum of $PEGMA_{17}$-b-$DEAEMA_{27}$. (c) GPC chromatogram of $PEGMA_{17}$-b-$DEAEMA_{27}$.
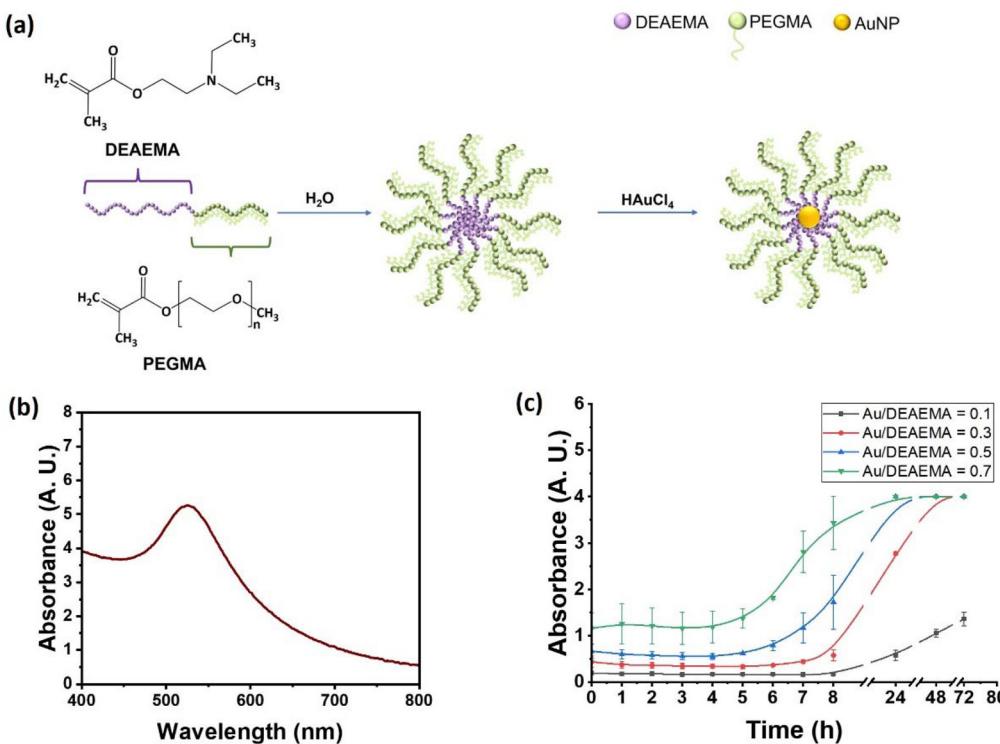
Table 1 Theoretical chemical structures, dispersity, theoretical and experimental molecular weights and compositions of the copolymers and its precursor of $PEGMA_{17}$-b-$DEAEMA_{27}$

Theoretical polymer structure	MM$^{theor.}$ (g mol^{-1})	M_n [a] (g mol^{-1})	$Đ$ [a]	OEGMA300-DEAEMA (w/w%)	
				Theoretical	Experimental [b]
$PEGMA_{17}$	5100	5400	1.13	100–00	100–00
$PEGMA_{17}$-b-$DEAEMA_{27}$	10 100	10 200	1.14	50–50	50–50

[a] These values were determined by GPC analysis before precipitation. [b] These values were determined by ^{1}H NMR analysis before precipitation.

overall particle. Given that all tested HAuCl$_4$: DEAEMA ratios generated viable nanoparticles, the 0.7 ratio (hydrodynamic size ~44 nm) was selected for use, in order to give the largest quantity of gold per nanoparticle and hence the greatest contrast in X-CT imaging.

The selected nanoparticles were further characterized by transmission electron microscopy (TEM, Fig. 3), which primarily images the gold nanoparticle core excluding the corona. These gold cores were confirmed as spherical in shape, with a modal diameter of 12 nm (Fig. 3b). Finally, to confirm that the

Fig. 2 (a) Schematic illustration of the self-assembly behaviour of PEGMA$_{17}$-b-DEAEMA$_{27}$, which is a diblock copolymer, with the hydrophobic part forming the centre of the micelle. The subsequent formation of AuNPs by the addition of HAuCl$_4$ is also presented. The DEAEMA and PEGMA units are show in green and purple respectively. (b) UV-vis histogram of polymeric AuNP. (c) Graph showing the kinetics of solutions containing PEGMA$_{17}$-b-DEAEMA$_{27}$ mixed with gold at different HAuCl$_4$: DEAEMA molar ratio, showing absorbance at a 520 nm wavelength over time. The markers and error bars show mean and standard deviation of three measurements at each time point and condition.

Table 2 Zeta potential and hydrodynamic diameters of PEGMA$_{17}$-b-DEAEMA$_{27}$ and polymeric AuNP with different polymer structures and molar ratios of HAuCl$_4$ to DEAEMA, at pH 7.5

Theoretical polymer structure	Ratio of Au : DEAEMA (w/w%)	Zeta potential (mV)	Diameter by DLS (nm)
PEGMA$_{17}$-b-DEAEMA$_{27}$	0		20.91
PEGMA$_{17}$-b-DEAEMA$_{27}$	0.1	8.24	45.87
	0.3	9.44	50.69
	0.5	18.6	41.13
	0.7	23.9	43.52

gold nanoparticles do indeed sit within polymer micelle coronas as predicted, negative staining by uranyl acetate was used to visualize the polymer corona around each nanoparticle (Fig. 3c). The visualized corona size was ~2 times greater than the gold core, consistent with the expectation from DLS measurements (albeit the negative staining measurement used a dried sample).
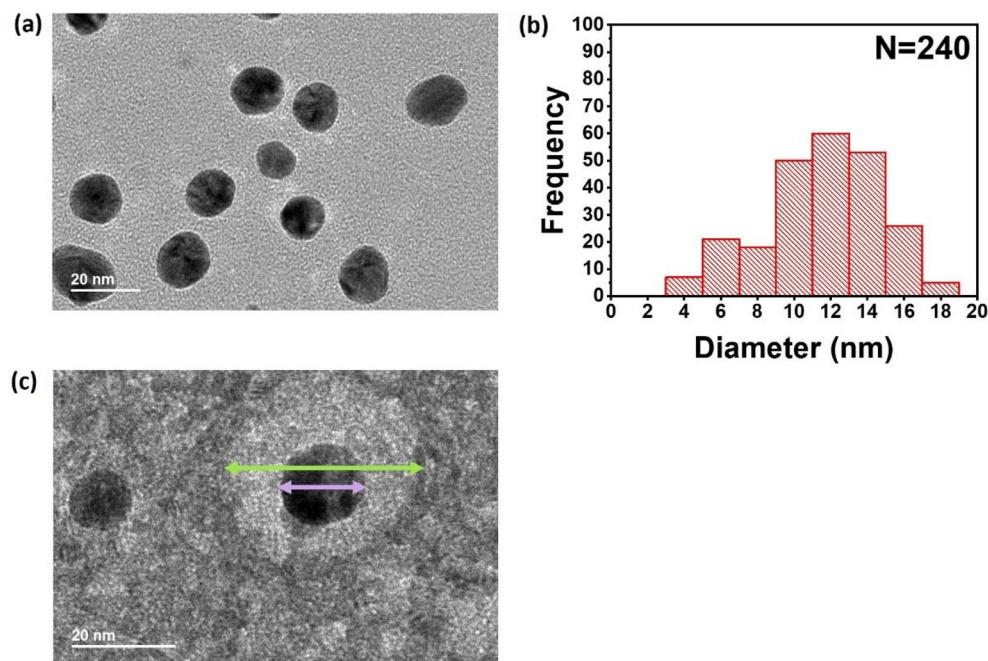
Micelle-templated gold nanoparticles are stable at high ionic strength and in the soil environment

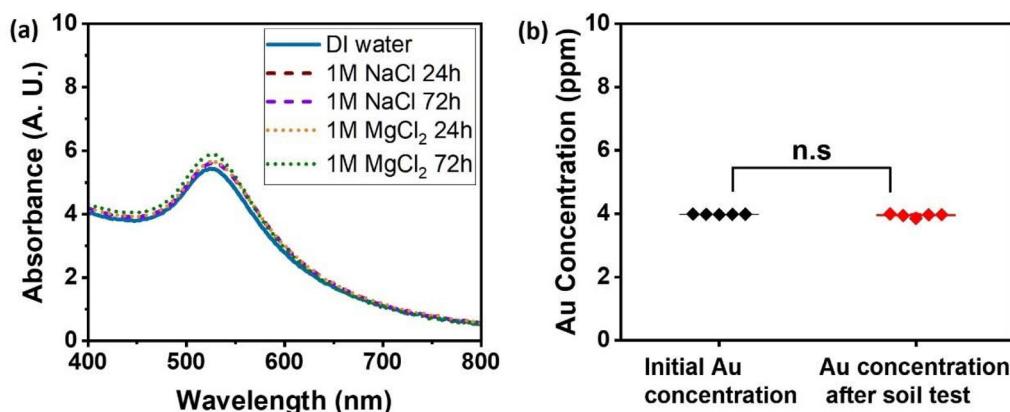Since the soil environment contains significant, and highly varying, quantities of salt, we first confirmed that the polyPEGMA corona is adequate to stabilize the nanoparticles against flocculation at high ionic strength, I. This was tested by mixing with equal volumes of 1 M solutions of NaCl (resulting in a final $I = 0.5$ M) and MgCl$_2$ (resultant $I = 1.5$ M). UV-vis data show that no discernible aggregation has occurred, with the traces the same as in salt-free water (Fig. 4a). This confirms that the stabilizing effect of the polyPEGMA with bottlebrush-like morphology is extremely strong, and clearly sufficient for the ionic strengths typically found in the soil environment, $e.g.$ 127 mM for an Australian soil sample (calculated from data in ref. 47).

As well as high-ionic-strength flocculation, which is a risk in many applications, soil poses a unique challenge as nanoparticles could stick to soil mineral surfaces, which in particular include aluminosilicate and metal oxide surfaces that can present both positive and negative charges. Furthermore, the potential interaction with of soil organic matter is unknown. To investigate the stability of the micelle-templated gold nanoparticles against these effects, a nanoparticle solution was mixed with an air-dried sandy-loam textured agricultural soil (Eutric Cambisol), to create a slurry which was then shaken for 24 h. The soil solids were then removed by centrifugation. Analysis of the supernatant, $i.e.$ the micelle-templated gold nanoparticle solution showed no significant reduction in the gold concentration compared with the original solution

Fig. 3 (a) Bright field TEM image of the polymeric AuNP. (b) Size distribution of polymeric AuNP from TEM image (a). (c) Bright field TEM image of polymeric AuNP with background stained with uranyl acetate. The green arrow indicates the polymer corona while the purple arrow indicates the AuNP core.
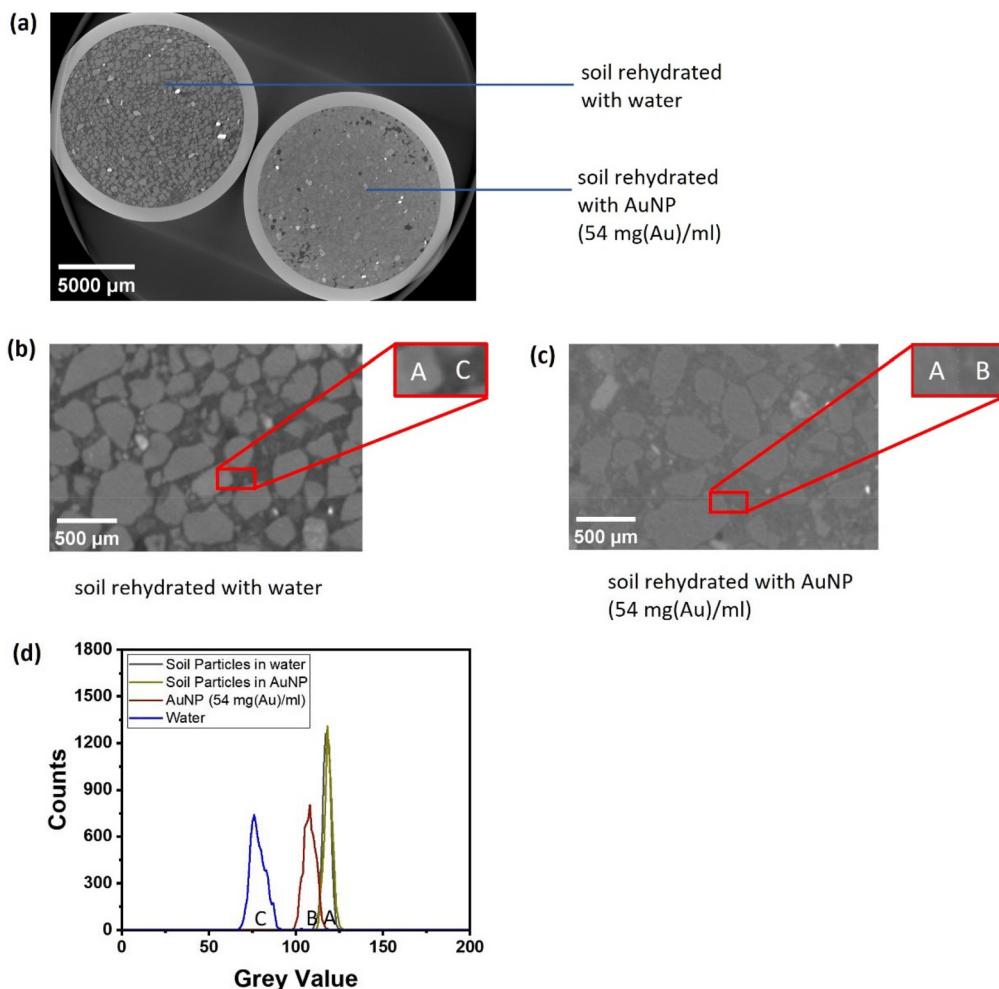

Fig. 4 (a) UV-vis histogram of polymeric AuNP in strong ionic solution (mixed in equal volume with 1 M NaCl solution and 1 M MgCl$_2$ solution, giving final ionic strengths 0.5 M and 1.5 M respectively). (b) ICP results for gold concentration in polymeric AuNP solution before and after stability test in soil environment, n.s indicates no significant difference ($p > 0.05$; t-test). $N = 5$ samples for both conditions.

(Fig. 4b). This indicates that essentially all the nanoparticles remain in solution, and essentially none have adsorbed to or been taken up by the solid mineral or organic phases, exactly as is required for application in imaging the soil aqueous phase.

Labelling of the soil aqueous phase with high stability and contrast in μX-CT

To evaluate the performance of the micelle-templated nanoparticles as contrast agents, the same soil was rehydrated with water and alternatively with an aqueous solution of the nano-

particles (54 mg(Au) ml^{-1}), in two otherwise identically prepared tubes. These were then imaged side-by-side using a μX-CT (Zeiss XRM-510 instrument with 80 keV X-ray, voxel size 14.05 μm, with image reconstruction performed using Zeiss Reconstructor Software; full details in Methods). A horizontal slice through the reconstructed 3D image is shown in Fig. 5a with blow-ups of the selected regions in Fig. 5b and c. (Note that greyscale value in the X-CT images represents the level of X-ray attenuation in arbitrary units, so that more strongly attenuating pixels are shown as brighter, which is the standard convention.) It can be observed that the aqueous phase exhi-

© 2025 The Author(s). Published by the Royal Society of Chemistry

RSC Appl. Polym., 2025, **3**, 1596–1612 | **1601**

Fig. 5 (a) The μX-CT image of DI water fully saturating soil (left) and polymeric AuNP suspension, at a concentration of 54 mg(Au) mL^{-1}, fully saturating soil (right). (b) A small XCT region of DI water fully saturating soil, in which shown the contrast between soil particles (A) and DI water (C). (c) A small XCT image region of a polymeric AuNP suspension, at a concentration of 54 mg(Au) mL^{-1}, fully saturating soil. The polymeric AuNP suspension (B) can be easily distinguished from the soil (A). (d) This contrast among the attenuation of soil (A) and DI water (C) is also visible in the histogram of grey values, also compare with the attenuation of polymeric AuNP (B).

bits a substantially higher greyscale value (on an 8-bit scale) in the sample where it is labelled with gold nanoparticles, in comparison with the sample where it is not. This is evidently due to the higher average electron density of the gold-labelled area, arising from the fact that gold's atomic mass is so much higher than the light elements otherwise present in this phase. The relative greyscale (X-ray attenuation) values of the different phases are quantitatively compared in Fig. 5d. It can be seen that the nanoparticle-labelled aqueous phase sits between the values of the unlabelled aqueous phase, and soil, and can be distinguished from both. Indeed, although the value of the labelled water phase is clearly closer to that of soil than the unlabelled water, it is still possible to segment the two phases (Fig. S1).

Importantly, the labelled aqueous phase shows as a continuous grey region in the image. This means that the micelle-templated nanoparticles are acting as intended: as a contrast agent. Individual nanoparticles are clearly far smaller than the voxel size, and are not resolved: rather each voxel of the aqueous phase contains many nanoparticle that raise its average electron attenuation level. No aggregates are visible, so the colloidal stability of the nanoparticles is intact at least to the extent necessary for this application, which is expected given their very high stability in electrolyte solutions (see above). Furthermore, the nanoparticles do not accumulate or deposit at the edges of the mineral particles, as the mineral phase particles do not exhibit bright edges. Again this is an indication that the stabilizing PEGMA corona is functioning as intended. Indeed, this is a potentially more challenging requirement than the avoidance of flocculation, as mineral phases can present both positive and negative charges. Furthermore, the stabilization of nanoparticles against mineral phases has been to date much less investigated than stabilization against colloidal flocculation.
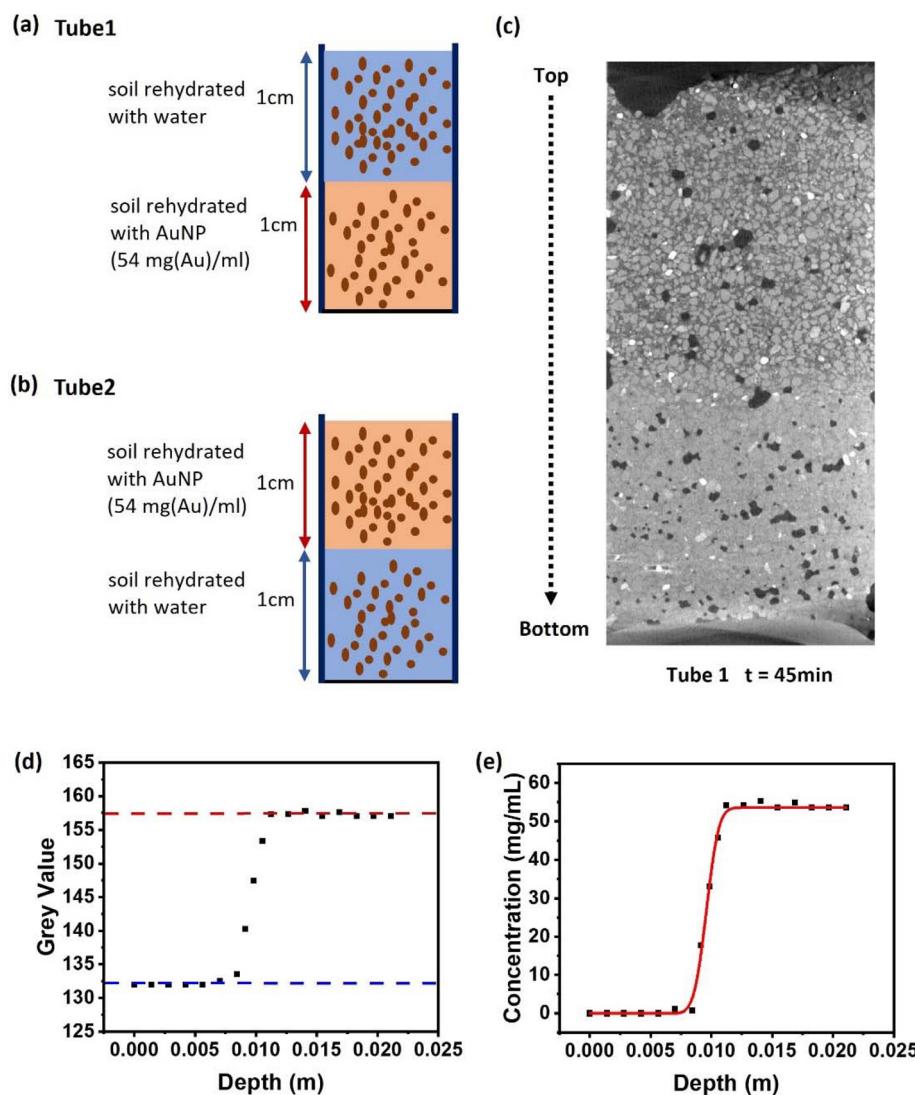
Transport in the soil microenvironment µX-CT imaging of nanoparticle diffusion

A key use of contrast agents in the soil microenvironment is to image transport processes including diffusion and the flow of water through the pore network. Here, we have characterized the diffusion of the micelle-templated gold nanoparticles within a soil microenvironment. The ability to use a contrast agent to investigate flow processes depends on its diffusion rate: if the diffusion rate is faster than the flow/transport process being investigated, then the contrast agent will spread rapidly throughout the sample, and it will not be possible to characterize water transport. Hence the diffusion rate provides a lower limit on the flow rates to be investigated. In principle a nanoparticle system should be superior to a small-molecule or ionic contrast agent, because in general larger objects diffuse more slowly. Here we test that for the micelle-templated nanoparticle system.

Measurement of diffusion followed a classical approach also used in *e.g.* polymer melts,[48] where a labelled material is brought into direct contact with an identical but unlabelled material, creating a sharp step-function concentration profile of the labelling reagent. Diffusion then causes this initially sharp interface to broaden over time, either more or less rapidly according to the magnitude of the diffusion constant. Here, a tube (glass, with 12 mm diameter) was filled to a

Fig. 6 (a) A Schematic representation of tube 1 with 1 cm height of soil rehydrated with DI water on the top and 1 cm of soil rehydrated with polymeric AuNP on the bottom. (b) A schematic representation of tube 2 with 1 cm height of soil rehydrated with polymeric AuNP on the top and 1 cm soil rehydrated with ultrapure water on the bottom. (c) An µX-CT image region of tube 1 in Z axis at 45 min after the diffusion started. (d) The grey-scale value of the liquid phase in different depth of tube 1, recorded at 45 min after the diffusion started. The red and blue dashed line are the grey-scale values of polymeric AuNP solution and DI water from the extreme end of the tubes, respectively. (e) The fitted diffusion curve of the liquid phase in different depths of tube 1, recorded at 45 min after the diffusion started. The black markers represent the grey value of the liquid phase at each depth, the red line is the fitted diffusion curve by fitting the black markers using eqn (1).

© 2025 The Author(s). Published by the Royal Society of Chemistry

RSC Appl. Polym., 2025, **3**, 1596–1612 | **1603**

depth of 200 mm with soil that had been rehydrated with an aqueous solution of the micelle-templated gold nanoparticles (54 mg(Au) ml^{-1}), followed by a second layer of equal thickness consisting of soil that had been rehydrated with water (ultrapure 18.2 MΩ) (Fig. 6a, schematic image on left). A second tube was prepared the other way up, with the gold nanoparticle-labelled soil forming the bottom layer, as a control to ensure the observed effects result from diffusion rather than gravity (Fig. 6b, schematic image on left, see also Fig. S4). The tubes were placed in the μX-CT instrument and imaged using a set of parameters that enabled a scan to be taken every ~35 minutes. They were then imaged continuously for 24 hours by which time substantial diffusion had occurred. The images were rendered (Zeiss Reconstructor Software), generating full 3D-reconstructions, through which vertical and horizontal slices were taken for visualization and analysis. Vertical slices taken at the beginning (45 min, times stated refer to the middle point of the measurement) and end (1457 min) of the 24 hours period are shown in Fig. 6a and b (right-hand images).

The concentration of the polymer-templated gold nanoparticles was determined as a function of the vertical position within the tube. Briefly, 2D slice-images were generated at regularly-spaced vertical positions. For each of these, the average grey-scale value was taken for representative areas of pore-water. This generated a depth profile of grey-scale (Fig. 6c), which was converted into a depth profile of gold concentration by calibrating against the known concentrations of gold in the end-regions, *i.e.* 0 and 54 mg(Au) ml^{-1}, shown as dashed lines in Fig. 6c for an initial time point (45 min); the resulting concentration profile is Fig. 6d.

Consider an example of the initial condition, as nearly as it can be measured due to set-up and scan time, Fig. 6d (black markers show measured data). The sharp interface between regions hydrated with unlabelled and gold-labelled water can clearly be seen. The evolution of this depth profile was followed over time (Fig. 7). The process of diffusion broadens the interface over the 24 hours period. Conceptually, this indicates the speed of diffusion, since a more rapid diffusive process would lead to a more rapid broadening of the interface.

Mathematically, this experiment is modelled by considering diffusion in two semi-infinite half-spaces, for an initial condition of a step-function concentration profile, with the step at
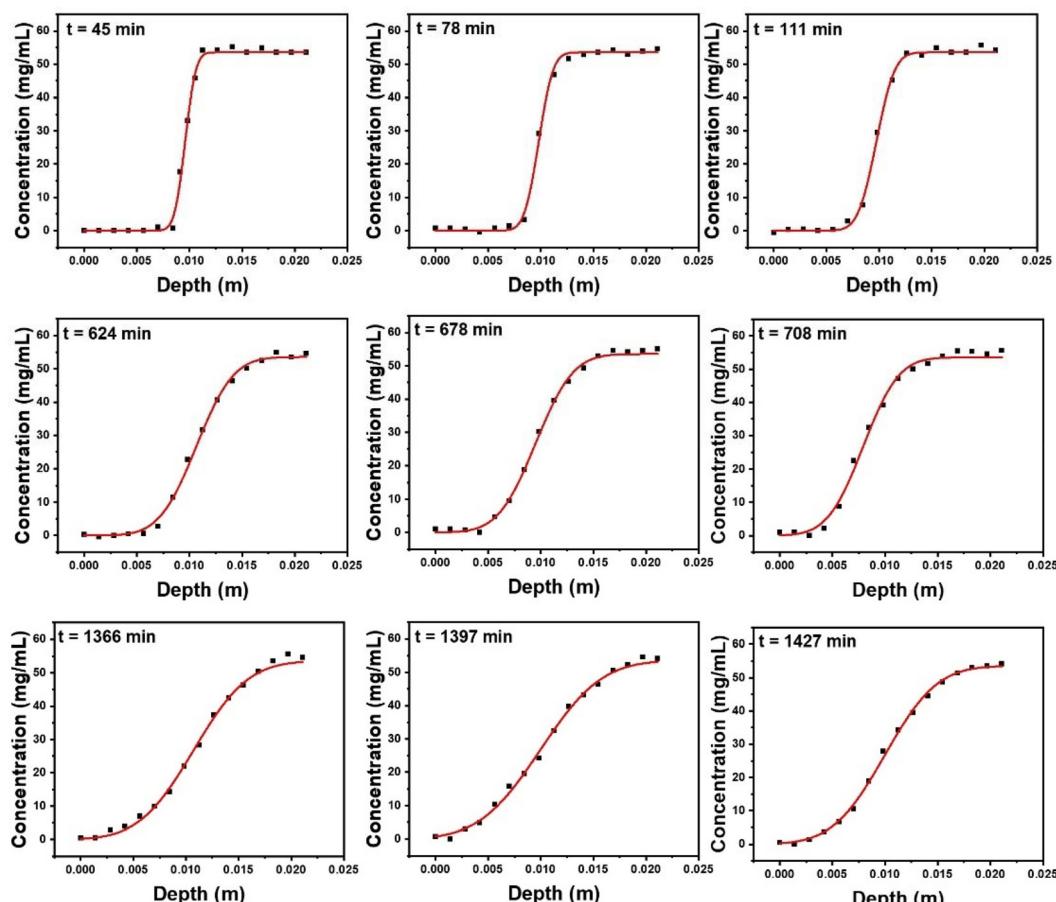

Fig. 7 The fitted diffusion curve of the liquid phase in different depths of tube 1 at different stage of the experiment, recorded at 45 min, 78 min, 129 min, 624 min, 678 min, 708 min, 1366 min, 1397 min and 1427 min after the diffusion started.

$d = d_0$ where d is the spatial direction perpendicular to the interface, in our case the vertical position along the tube. This has previously been solved analytically,[49] giving a solution,
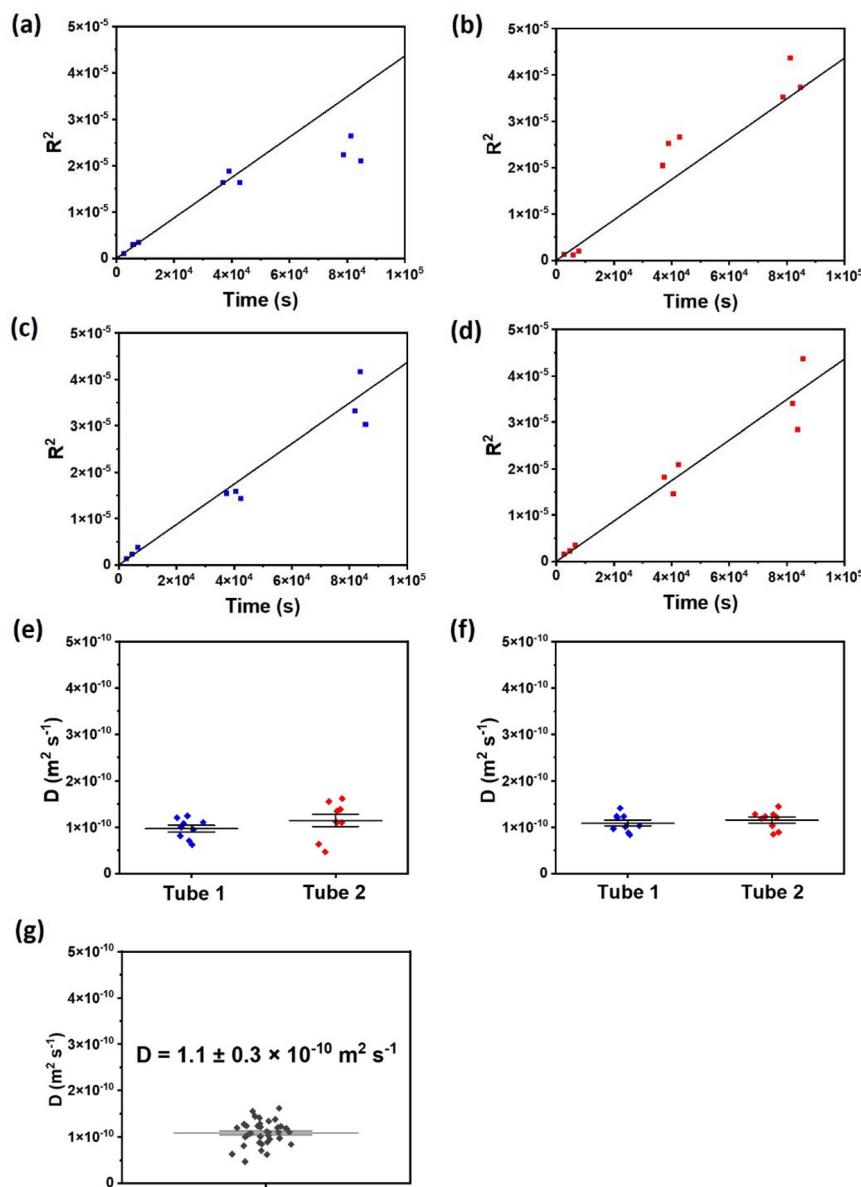
$$C(d, t) = \frac{C_0 \times \mathrm{erfc}\left[\dfrac{(d - d_0)}{2 \times \sqrt{Dt}}\right]}{2}, \qquad (1)$$

where t is the time elapsed since the initial sharp-interface condition, D is the diffusion constant, C_0 is the concentration in the higher-concentration zone, and erfc() is the complementary error function. We use this solution to generate a simplified equation that expresses the expected shape of the

Au concentration as a function of vertical position at a given time,

$$C(d) = \frac{C_0}{2} \mathrm{erfc}\left[\frac{d - d_0}{R}\right], \qquad (2)$$

where R is defined by $R^2 = 4Dt$, as a measure of the interfacial width. Using this equation, the concentration profiles were fitted and parameterized for each time point. Fits are indicated by red lines in Fig. 7, and demonstrate that this is a good model for the observed process. A total of 9 data sets at varying times were analysed, which were at the beginning (at 45 min, 78 min and 111 min), in the middle (at 624 min,

Fig. 8 Quantification of diffusion of micelle-templated gold nanoparticles in soil. The fitted interface width, R, as a function of time, t, for (a) tube 1 in the first diffusion experiment; (b) tube 2 in the first diffusion experiment; (c) tube 1 in the second diffusion experiment; (d) tube 2 in the second diffusion experiment. The distribution of diffusion constants (D) of (e) tube 1 and tube 2 in the first diffusion experiment; (f) tube 1 and tube 2 in second diffusion experiment; (g) all values of D from the two diffusion experiments.

678 min and 708 min) and at the end of the experiment (at 1366 min, 1397 min and 1427 min), with the fitted concentration profiles becoming broader flatter over time, in accordance with the data. The experiment was repeated twice, giving a total of four samples/tubes measured. We note in passing that labelled water is clearly distinguished from unlabelled water at concentrations at least down to ~5 mg ml^{-1} Au.

To confirm that Fickian diffusion accurately describes the process, the interfacial width, R, is displayed as a plot of R^2 vs. t, which is expected to generate a linear relationship (Fig. 8a–d, plotted separately for each sample tube). It can be seen that this relationship holds well across the four experiments and three time points. A sole exception is that the interfacial broadening was slower than expected at the longest times in tube 1 (we note in this context that some sample variation is expected in soil, and that the model is likely to be least accurate at the longest time-scales, where the broadening effect may begin to reach the ends of the tubes and hence the boundary conditions inherent in the analytic solution are no longer valid). Based on this agreement, we used R to infer the diffusion constants for the different experiments, based on $R^2 = 4Dt$.

Hence, the diffusion constants are determined separately in each of the four experiments (Fig. 8e, f and Table 3). The four samples measured show a high level of consistency, with in particular no substantial differences between tubes where the gold was on the top vs. the bottom, confirming that gravitational effects did not have a significant impact.

The overall average diffusion constant for the micelle-templated gold nanoparticles in this soil system is determined to be $1.1 \pm 0.3 \times 10^{-10}$ m^2 s^{-1}. We note that this is a relatively slow diffusion, in comparison with ionic species in soil such as K$^+$ (10^{-7}–10^{-8} m^2 s^{-1}) and NO$_3^-$ (10^{-6}–10^{-7} m^2 s^{-1}).[50] This is in line with what one would expect from a much larger nanoparticle reagent, and indicates that these nanoparticles can be effective tracers for flow experiments.

Comparison with single-particle diffusion constant

The bulk diffusion co-efficient in the soil environment can be compared with the single particle diffusion co-efficient for the gold nanoparticles in water. The latter was measured by dynamic light scattering, DLS. Although DLS is typically used to estimate particle size, as we have done earlier, the data found by measuring thermal fluctuations that can alternatively be processed to output a diffusion constant. The measured diffusion constant, D_{single} of the micelle-templated gold nanoparticles in dilute solution (3.24 mg(Au) ml^{-1}) is 1.50×10^{-11} m^2 s^{-1} (Table 4). Intriguingly this is nearly an order of magnitude smaller than the bulk diffusion constant measured in soil. This contradicts intuitive expectations, since one would expect the more respected space of the soil environment to lower rather than raise the speed of diffusion.

In fact, it is possible for bulk diffusion to occur more rapidly than single-particle diffusion, when the concentration of particles used is high enough to induce crowding, according to a mechanism that has been outlined theoretically (shown schematically in Fig. 9b).[49] In the canonical case where particles are relatively dilute, then each particle can move with equal freedom in each direction (Fig. 9a). This means that each particle executes a random walk, ultimately leading to diffusion with a bulk diffusion constant equal to the single-particle constant. However when the particle concentration is relatively high, then crowding effects mean that movement up a concentration gradient (towards the crowded region) is disfavoured, whereas movement down the concentration gradient, towards the less crowded region, is easier. This asymmetry means that the particles spread out into the lower concentration region faster than would otherwise be expected, meaning that bulk diffusion measurements such as we have conducted here will lead to higher measured diffusion constant, consistent with our observed results.

Table 4 Hydrodynamic diameter and single particle diffusion coefficient of AuNP measured by DLS

Concentration of AuNP (mg(Au) mL^{-1})	AuNP size (nm)	Diffusion coefficient (m^2 s^{-1})
3.24	32.7	1.5×10^{-11}

Fig. 9 (a) A schematic representation of single particle diffusion of polymeric AuNP measured by DLS. Pink spheres represent the polymeric AuNP. Pink spheres represent the polymeric AuNP. (b) A schematic representation of diffusion of polymeric AuNP in soil measured by μX-ray CT. Red spheres represent the polymeric AuNP.

Table 3 Diffusion constants from each tube in the two diffusion experiments, stated as mean ± standard deviation

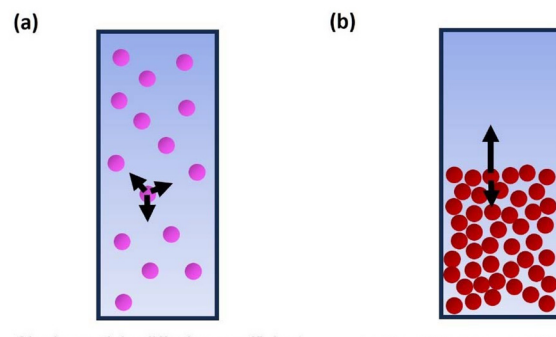| Experiment	Tube number and orientation	Diffusion constants (m^2 s^{-1})
First diffusion experiment	Tube 1 (AuNP labelled water at bottom)	$0.9 \pm 0.2 \times 10^{-10}$
	Tube 2 (AuNP labelled water at top)	$1.2 \pm 0.4 \times 10^{-10}$
Second diffusion experiment	Tube 1 (AuNP labelled water at bottom)	$1.1 \pm 0.2 \times 10^{-10}$
	Tube 2 (AuNP labelled water at top)	$1.2 \pm 0.2 \times 10^{-10}$

Conclusion

We have developed polymer-templated gold nanoparticles as a contrast agent for µX-CT imaging in soil, exploiting the known biocompatibility of gold in comparison with competitors such as iodine-based reagents or other heavy metals. The particle synthesis is a single step process that can be performed at high concentrations. In combination with the production of diblock copolymers by GTP, this generates a nanoparticle system that is scalable and practicable for soil applications. The polymer-templated gold nanoparticles show high stability in the soil environment, and enable labelling of the soil aqueous phase with good contrast in µX-CT. Diffusion measurements confirmed the ability of this new contrast system to be used in transport studies, and reveals that diffusion is slower than typical ionic species, confirming the system's potential to be used as a flow tracer. Taken together, these results show polymer-templated nanoparticles to be a high-class contrast agent for tracing flow and transport in µX-CT. The use of PEGylated nanoparticles for enhanced bioinertness is a strength of the technology, although the impact on specific microbial communities will need to be determined by direct experiment. This nanoparticle contrast agent will enable the direct imaging of water transport in soil, elucidating the microscale mechanisms of transport, with the potential for long-term benefit to agricultural and environmental science.

Materials and methods

Materials

Poly(ethylene glycol)methyl ether methacrylate (PEGMA, MM = 300 g mol^{-1}), 2-(diethylamino)ethyl methacrylate (DEAEMA, 99%, MM = 185.26 g mol^{-1}) were monomers used to synthesise the diblock copolymer. Calcium hydride (CaH$_2$, ≥90%), aluminium oxide activated basic (Al$_2$O$_3$·KOH), 2,2-diphenyl-1-picrylhydrazyl (DPPH), tetrahydrofuran (THF, anhydrous, ≥99.9%, inhibitor-free) were used to purify monomers, anhydrous THF was also used as a polymer synthesis solvent. 1-Methoxy-1-trimethylsiloxy-2-methyl propene (MTS, polymerisation initiator), tetrahydrofuran (THF, HPLC grade, polymerisation solvent, ≥99.9%) mixed with 5 vol% triethylamine (99%), deuterated chloroform (CDCl$_3$, 99.8%) were used as the initiator, solvent for gel permeation chromatography (GPC) and solvent for proton nuclear magnetic resonance spectroscopy (^{1}H NMR), respectively. Other solvents used include hexane, methanol and acetone (analytical grade), they were used for polymer precipitation, polymerization termination and glassware-washing, respectively. The catalyst used in polymer synthesis, tetrabutylammonium bibenzoate (TBABB), was previously synthesized from tetrabutylammonium hydroxide (40% in water) and benzoic acid (99.5%), according to Dicker's report,[51] and kept dried under argon until use. Gold (III) chloride trihydrate (MM = 393.83 g mol^{-1}) was the gold source for gold nanoparticle formation. Sodium hydroxide (NaOH, 97%) and hydrochloric acid solution (volumetric, 1 M) were used for titration and adjusting pH. Sodium chloride (NaCl) and magnesium chloride (MgCl$_2$) were used for gold nanoparticles stability testing. ICP calibration used a purchased Gold Standard. Chemicals listed above were from Sigma Aldrich Co Ltd, UK, except for hexane and tetrabutylammonium hydroxide, from Acros Organics, UK.

Purification of polymerization reagents

DEAEMA was passed through a basic aluminium oxide column twice to remove any protic impurities. To eliminate moisture, the DEAEMA was mixed with CaH$_2$ and stirred for 2 hours at least 3 days before polymerization. DPPH was also added as a free-radical inhibitor. For PEGMA, a 50% vol PEGMA and 50% vol THF solution was prepared. This was passed through the basic aluminium oxide column twice, then stirred under argon with CaH$_2$ for two hours. When finished, DEAEMA and PEGMA solution with THF were purged with argon and refrigerated. DEAEMA and MTS were distilled one day before polymerisation to remove the free-radical inhibitor and any other impurities, under vacuum to eliminate moisture. Distillation was not possible for PEGMA as a high molar mass monomer.

Diblock copolymer synthesis and recovery

The diblock copolymer PEGMA$_{17}$-b-DEAEMA$_{27}$ was targeted at 10 000 g mol^{-1} with 70 : 30 wt% composition of DEAEMA to PEGMA. It was synthesised via sequential GTP. The exothermic polymerization reaction was monitored using a digital thermometer attached to the bottom of the flask. The exothermic polymerization reaction meant that the temperature increased while the monomer was polymerizing, and it started dropping when all the monomer had converted to the polymer, thus allowing the monitoring of the sequential polymerization. First, 10 mg of TBABB was added into a 250 mL round bottom flask filled with Argon, then 62.88 mL anhydrous THF was injected into the flask. Followed by injection of 0.5 mL freshly distilled MTS. Then the first monomer was added, 23.44 mL PEGMA (23.44 mL in 50 v/v% in THF, 12.31 g, 0.041 mol). The temperature started to increase from 21.5 to 31.5 °C. When the polymerization of the first monomer was completed, two samples were taken out from the reaction flask for GPC and ^{1}H NMR. Then DEAEMA was added (13.35 mL, 12.31 g, 0.066), whereupon the temperature increased again from 23.8 to 34.9 °C; two 0.1 ml samples were then taken for GPC and ^{1}H NMR. As GTP is highly moisture-sensitive, the flask was kept sealed by a rubber septum and purged with inert argon gas each time after materials were added or taken. After the polymerisation was complete, polymer was transferred to hexane drop by drop for precipitation, to remove any undesired low MM molecules and catalyst. Solvents were then removed, and the precipitated polymers left in a vacuum oven to dry at room temperature for at least a week. The polymers were then collected into vials; liquid nitrogen cooling was used to aid this transfer.

© 2025 The Author(s). Published by the Royal Society of Chemistry

RSC Appl. Polym., 2025, **3**, 1596–1612 | **1607**

Diblock copolymer characterisation: gel permeation chromatography (GPC)

To determine the molecular mass distribution, molar mass and degree of polymerisation (DP) of the diblock copolymer, GPC was conducted (Agilent SECurity GPC system, Agilent Technologies UK Ltd, Shropshire, UK, with a Polymer Standard Service (PSS) SDV analytical linear M column). This system is equipped with a "1260 Iso" isocratic pump and an Agilent 1260 refractive index (RI) detector (plotted in Fig. 1c is the raw normalised RI signal). The mobile phase was tetrahydrofuran (THF) with 5% vol trimethylamine (Et$_3$N) (flow rate 1 ml min^{-1}). The added Et$_3$N acts as a mild base to avoid DEAEMA absorption in the column. The column was calibrated using linear poly(methyl methacrylate) (PMMA) standard samples of MM 2000, 4000, 8000, 20 000, 50 000, and 100 000 g mol^{-1}, (Sigma Aldrich Co Ltd, UK). The samples were prepared by mixing 10 mg of polymer and 1 mL of GPC solvent (THF with 5% Et$_3$N), and filtered before passing through the device to prevent blockage.

Diblock copolymer characterisation: proton nuclear magnetic resonance (^{1}H-NMR)

Chemical structures and compositions of all polymers were determined from ^{1}H-NMR spectra (JEOL 400 MHz NMR spectrometer, Bruker UK Ltd, Coventry, UK). Samples for ^{1}H-NMR taken during polymerization were dried overnight in a vacuum oven to remove the solvent, then dissolved in 650 μL CDCl$_3$. The weight percentage of DEAEMA and PEGMA were determined by calculating the integral ratio of the signal from the CH$_2$ ethyl group next to N and closer to ester at 2.6 ppm, to that of the methoxy peak at 3.35 ppm.

Diblock copolymer characterisation: pK_a and cloud point

Since the diblock copolymer was pH-sensitive, titration was conducted to find out the effective pK_a. Firstly, around 5 ml of 1 wt% solution was made. The pH meter (Hanna HI98103 pH checker) was calibrated before use. The polymer solution was adjusted to pH 2 by adding hydrochloric acid (1 M). 20 μL of sodium hydroxide solution (0.25 M) was repeatedly added to the polymer solution, with the pH recorded after each addition, continued until the solution reached pH 12. The pK_a was then determined by the titration curve (that can be found in Fig. S2) and it was taken as the pH were 50% of the amino groups are protonated.

The cloud points of the polymers were determined by heating 1 w/w% aqueous polymer solution (1 ml) in a water bath, with a heating rate of 1 °C min^{-1}. After an initial visual observation between 20 °C to 70 °C to determine the approximate range within which the cloud point observed, the experiment was repeated in this narrower range using turbidimetry. Specifically, the polymer solution transmittance was measured as a function of temperature (Cary 3500 Compact Peltier UV–Vis System, Agilent).

Synthesis of polymer-templated gold nanoparticles

To form polymer-templated gold nanoparticles, aqueous stock solutions of polymer and gold(III) chloride trihydrate (HAuCl$_4$) solution were prepared, each at 2 wt% concentration, and separately adjusted to pH 7.5 using sodium hydroxide (1 M) and hydrochloric acid (1 M) solution. Then the gold(III) chloride trihydrate solution was added into polymer solution with different molar ratios of HAuCl$_4$ to DEAEMA (0.1, 0.3, 0.5 and 0.7), with the polymer concentration of the final solution always set to 1 wt% by addition of water. The reaction mixture was covered by foil and shaken for 48 hours (IKA KS 260 basic shaker, 200 min^{-1}). Nanoparticle formation was monitored by UV-vis, with the measurement taken before and after the addition of gold solution, every hour in the following 8 hours, and then at 24 hours and 48 hours after addition.

Centrifugal filtration

Throughout this study polymer-templated nanoparticles were concentrated and rinsed where necessary using centrifugal filtration (Amicon® Ultra Centrifugal Filter, 10 kDa MWCO, Fisherbrand™ GT1R Centrifuge, 4000 rpm). Concentration was carried out by placing the nanoparticle solution in the upper part of the filter assembly, and using the centrifuge to selectively remove water until a desired volume is reached. Rinsing used the same approach but with successive steps of dilution with pure water or the desired aqueous solvent, followed by reconcentration to reduce the concentration of electrolyte or other small impurities.

Characterization of polymer-templated gold nanoparticles

The successful synthesis of polymeric AuNPs was easily observed visually by its wine-red colour. It was also confirmed by Ultraviolet-Visible Spectroscopy (UV-vis) using NanoDrop™ One^C Microvolume UV-Vis spectrophotometer (Thermo Fisher Scientific Inc., UK. 2 μl sample size).

Hydrodynamic diameters of polymer-templated nanoparticles and separately polymer micelles were measured by dynamic light scattering (DLS, Zetasizer Nano ZSP, Malvern, UK, solution at 1 wt% polymer in ultrapure water (18.2 MΩ cm) after rinsing to remove background electrolyte). The parameters used were 25 °C and backscatter angle of 173°. Each sample was measured three times and the reports gave the mean values. The same method was used to determine the averaged single-particle diffusion constant, D_{single}, as discussed in the text; this can be read out directly from the Zetasizer software and is related to the hydrodynamic diameter via the Stokes–Einstein relation,

$$D_{single} = \frac{k_B T}{6\pi\eta R_H},$$

where η is the solvent viscosity, R_H the hydrodynamic diameter, T the temperature, and k_B Boltzmann's constant.

The diblock copolymer solution was filtered prior to the measurement to remove bubbles (0.45 μm PTFE syringe filter). The zeta potential of polymer-templated gold nanoparticles

was also determined using the same instrument with the same parameters: in this case polymer-templated nanoparticles were additionally rinsed and re-concentrated by centrifugal filtration to eliminate any traces of electrolyte.

The gold cores of the polymer-templated gold nanoparticle constructs were imaged by transmission electron microscopy (TEM) (JEOL JEM-2100F). Samples were prepared by pipetting nanoparticle solution (10 μL, 3.4 mg ml^{-1}) onto holey-carbon grids. The solution was kept on the grid for 2 min, then excess liquid was removed from the backside using filter paper, before overnight drying (room temperature). Additionally, negative staining with uranyl acetate was used to visualize the polymer corona around the gold core. The TEM grid was glow discharged by Fischione NanoClean model 1070 before use. 10 μL polymer solution was pipetted on to the glow discharged grid, left for 2 min and removed extra polymer solution from the backside using filter paper. The grid was then negatively stained by one drop of 2% w/v uranyl acetate for 60 s. The stained TEM grid was air dry for at least 1 h at room temperature before use. Diameters of the gold nanoparticles were quantified from TEM images. First, particle area was measured by thresholding using the ImageJ function AnalyzeParticles, and then diameters were calculated by assuming spherical shape.

Assessment of polymer-templated gold nanoparticle stability in high ionic strength solution

UV-vis is widely used to determine gold nanoparticle stability, as individualized nanoparticles exhibit a characteristic spectrum with a single peak at ~520 nm, associated with their well-known wine-red colour. Upon aggregation, the visually observed colour changes to blue-black, and the peak shows a substantial flattening towards higher wavelengths.[52] UV-vis spectroscopy was measured using NanoDrop™ OneC Microvolume UV-Vis spectrophotometer, Thermo Fisher Scientific Inc, UK, 2 μL sample size. Polymer-templated gold nanoparticles (3.4 mg(Au) ml^{-1}) were respectively mixed with sodium chloride (NaCl) (1 M) and magnesium chloride (MgCl$_2$) solutions (1 M), in two separate experiments, to give resultant concentrations of 1.7 mg(Au) ml^{-1} for the nanoparticles and 0.5 M for each of the electrolytes. UV-Vis spectra were measured at 24 h and 72 h after mixing.

Assessment of polymer-templated gold nanoparticle stability in contact with soil

To determine the stability of polymer-templated gold nanoparticles in soil, inductively coupled plasma optical emission spectrometer (ICP-OES) was performed to determine the Au concentration before and after mixing with soil particles. The sample was prepared by 100 mg soil (air-dried sandy-loam textured agricultural soil (Eutric Cambisol)) mixed with 750 μL polymer-templated gold nanoparticle solution (47.06 mg(Au) ml^{-1}), then left shaken for 24 h (Agar Scientific rotary shaker, 6 rpm). The soil was pelleted by centrifugation (SIGMA 1-14 Microfuge, 2000 rpm/310 G), and a sample of supernatant (4.3 μl) removed for testing. As a control, an identical volume

of polymer-templated gold nanoparticle solution was shaken and tested in the same way, but without mixing with soil. Overnight digestion was conducted on both samples using aqua regia (25 μL aqua regia was added to each sample to digest and oxidize the AuNPs and the dissolved organic matter), the samples were diluted with ultrapure water the next day to measure Au concentration using iCAP 6000 Series ICP-OES Spectrometer (Thermo Fisher Scientific Inc, UK), calibrated using Gold Standard for ICP (Sigma Aldrich Co Ltd, UK) at concentrations of 0, 5, 10, 15, and 20 ppm.

μX-CT imaging

A Zeiss XRM-510 X-ray microscope was used for high-resolution *in situ* imaging. The X-ray energy was 80 keV, power 7 W, and the exposure time was set to 1.2 s. Samples were placed in soda glass tubes of dimensions 12 mm, and two tubes could be accommodated within a single scan. All tomograms were reconstructed into three-dimensional images using the Zeiss Reconstructor Software, and further quantification of 2D slices taken from the rendered model was performed using ImageJ. For measurements to investigate stability of nanoparticles, the scan time was 1 hour and 40 minutes. In time-resolved experiments to measure diffusion, the scan time was approx. 35 minutes, and the scans were repeated successively until the total time reached 24 h.

Concentration profile analysis

To plot the concentration profile, the μX-CT images were analysed in 2D slices with regularly-spaced vertical positions. A total of 16 positions were chosen (from slice 180 to slice 1680, with 100 slides between each position). At each position, the average grey-scale value was taken from 20 representative areas of the aqueous phase. The slice number was then converted to depth using the equation: $\text{Depth (m)} = \frac{\text{voxel size} \times \text{slice number}}{1\,000\,000}$ (the voxel size is 12.1043 μm for the first diffusion experiment, and 14.0537 μm for the second diffusion experiment). The grey-scale values of the liquid phase were plotted against the depth (m). The greyscale value was further converted to concentration by calibrating against the known concentrations of gold in the end regions of the images (0 and 54 mg(Au) ml^{-1}). The converted concentrations were used for subsequent analysis for fitting the diffusion profiles.

Author contributions

I. E. D., T. K. G., M. B., T. R. and D. L. J. designed the project. I. E. D., T. K. G. and M. B. supervised the work with assistance from T. R. and D. L. J. S. W. performed experiments and data analysis, with A. C., G. Z., Y. Z., M. J. S., B. Z. The manuscript was written by S. W. and I. E. D. with review and participation from all authors.

Conflicts of interest

There are no conflicts to declare.

Data availability

Supporting data is included within supplementary information (SI), or is available from the corresponding author on request.

Supplementary information is available. See DOI: https://doi.org/10.1039/d5lp00072f.

Acknowledgements

References

1 J. Bouma, The New Role of Soil Science in a Network Society, *Soil Sci.*, 2001, **166**(12), 874–879, DOI: 10.1097/00010694-200112000-00002.

2 D. A. Robinson, N. Hockley, E. Dominati, I. Lebron, K. M. Scow, B. Reynolds, B. A. Emmett, A. M. Keith, L. W. de Jonge, P. Schjønning, *et al.*, Natural Capital, Ecosystem Services, and Soil Change: Why Soil Science Must Embrace an Ecosystems Approach, *Vadose Zone J.*, 2012, **11**(1), DOI: 10.2136/vzj2011.0051.

3 W. E. H. Blum, Functions of Soil for Society and the Environment, *Rev. Environ. Sci. Bio/Technol.*, 2005, **4**(3), 75–79, DOI: 10.1007/s11157-005-2236-x.

4 F. S. Chapin III, J. McFarland, A. D. McGuire, E. S. Euskirchen, R. W. Ruess and K. Kielland, The Changing Global Carbon Cycle: Linking Plant–Soil Carbon Dynamics to Global Consequences, *J. Ecol.*, 2009, **97**(5), 840–850, DOI: 10.1111/j.1365-2745.2009.01529.x.

5 W. M. Post, W. R. Emanuel, P. J. Zinke and A. G. Stangenberger, Soil Carbon Pools and World Life Zones, *Nature*, 1982, **298**(5870), 156–159, DOI: 10.1038/298156a0.

6 S. Wiltshire and B. Beckage, Soil Carbon Sequestration Through Regenerative Agriculture in the U.S. State of Vermont, *PLoS Clim.*, 2022, **1**(4), e0000021, DOI: 10.1371/journal.pclm.0000021.

7 M. Krauss, M. Wiesmeier, A. Don, F. Cuperus, A. Gattinger, S. Gruber, W. K. Haagsma, J. Peigné, M. C. Palazzoli, F. Schulz, *et al.*, Reduced Tillage in Organic Farming Affects Soil Organic Carbon Stocks in Temperate Europe, *Soil Tillage Res.*, 2022, **216**, 105262, DOI: 10.1016/j.still.2021.105262.

8 T. J. Mattila, E. Hagelberg, S. Söderlund and J. Joona, How Farmers Approach Soil Carbon Sequestration? Lessons Learned From 105 Carbon-Farming Plans, *Soil Tillage Res.*, 2022, **215**, 105204, DOI: 10.1016/j.still.2021.105204.

9 I. M. Young and J. W. Crawford, Interactions and Self-Organization in the Soil-Microbe Complex, *Science*, 2004, **304**(5677), 1634–1637, DOI: 10.1126/science.1097394.

10 D. L. Jones and P. Hinsinger, The Rhizosphere: Complex by Design, *Plant Soil*, 2008, **312**(1), 1–6, DOI: 10.1007/s11104-008-9774-2.

11 L. G. Tumlinson, H. Liu, W. K. Silk and J. W. Hopmans, Thermal Neutron Computed Tomography of Soil Water and Plant Roots, *Soil Sci. Soc. Am. J.*, 2008, **72**(5), 1234–1242, DOI: 10.2136/sssaj2007.0302.

12 A. Carminati, A. B. Moradi, D. Vetterlein, P. Vontobel, E. Lehmann, U. Weller, H.-J. Vogel and S. E. Oswald, Dynamics of Soil Water Content in The Rhizosphere, *Plant Soil*, 2010, **332**(1), 163–176, DOI: 10.1007/s11104-010-0283-8.

13 H. H. Rogers and P. A. Bottomley, In Situ Nuclear Magnetic Resonance Imaging of Roots: Influence of Soil Type, Ferromagnetic Particle Content, and Soil Water, *Agron. J.*, 1987, **79**(6), 957–965, DOI: 10.2134/agronj1987.00021962007900060003x.

14 A. Pohlmeier, A. Oros-Peusquens, M. Javaux, M. I. Menzel, J. Vanderborght, J. Kaffanke, S. Romanzetti, J. Lindenmair, H. Vereecken and N. J. Shah, Changes in Soil Water Content Resulting from Ricinus Root Uptake Monitored by Magnetic Resonance Imaging, *Vadose Zone J.*, 2008, **7**(3), 1010–1017, DOI: 10.2136/vzj2007.0110.

15 J. R. Helliwell, C. J. Sturrock, K. M. Grayling, S. R. Tracy, R. J. Flavel, I. M. Young, W. R. Whalley and S. J. Mooney, Applications of X-ray Computed Tomography for Examining Biophysical Interactions and Structural Development in Soil Systems: a Review, *Eur. J. Soil Sci.*, 2013, **64**(3), 279–297, DOI: 10.1111/ejss.12028.

16 C. Villa, B. Frohlich and N. Lynnerup, Chapter 7 - The Role of Imaging in Paleopathology, in *Ortner's Identification of Pathological Conditions in Human Skeletal Remains*, ed. J. E. Buikstra, Academic Press, 3rd edn, 2019, pp. 169–182.

17 S. J. Mooney, T. P. Pridmore, J. Helliwell and M. J. Bennett, Developing X-ray Computed Tomography to Non-invasively Image 3-D Root Systems Architecture in Soil, *Plant Soil*, 2012, **352**(1), 1–22, DOI: 10.1007/s11104-011-1039-9.

18 S. H. Anderson, R. L. Peyton and C. J. Gantzer, Evaluation of Constructed and Natural Soil Macropores Using X-ray Computed Tomography, *Geoderma*, 1990, **46**(1), 13–29, DOI: 10.1016/0016-7061(90)90004-S.

19 R. I. Al-Raoush and C. S. Willson, Extraction of Physically Realistic Pore Network Properties from Three-dimensional Synchrotron X-ray Microtomography Images of Unconsolidated Porous Media Systems, *J. Hydrol.*, 2005, **300**(1), 44–64, DOI: 10.1016/j.jhydrol.2004.05.005.

20 J. Lipiec and R. Hatano, Quantification of Compaction Effects on Soil Physical Properties and Crop Growth, *Geoderma*, 2003, **116**(1), 107–136, DOI: 10.1016/S0016-7061(03)00097-1.

21 J. W. Hopmans, T. Vogel and P. D. Koblik, X-ray Tomography of Soil Water Distribution in One-Step Outflow Experiments, *Soil Sci. Soc. Am. J.*, 1992, **56**(2), 355–362, DOI: 10.2136/sssaj1992.03615995005600020004x.

22 A. Kaestner, M. Schneebeli and F. Graf, Visualizing Three-dimensional Root Networks Using Computed Tomography, *Geoderma*, 2006, **136**(1), 459–469, DOI: 10.1016/j.geoderma.2006.04.009.

23 P. J. Gregory, D. J. Hutchison, D. B. Read, P. M. Jenneson, W. B. Gilboy and E. J. Morton, Non-invasive Imaging of Roots with High Resolution X-ray Micro-tomography, *Plant Soil*, 2003, **255**(1), 351–359, DOI: 10.1023/A:1026179919689.

24 S. R. Tracy, J. A. Roberts, C. R. Black, A. McNeill, R. Davidson and S. J. Mooney, The X-factor: Visualizing Undisturbed Root Architecture in Soils Using X-ray Computed Tomography, *J. Exp. Bot.*, 2010, **61**(2), 311–313, DOI: 10.1093/jxb/erp386, acccessed 10/5/2023.

25 S. J. Mooney, C. Morris and P. M. Berry, Visualization and Quantification of the Effects of Cereal Root Lodging on Three-Dimensional Soil Macrostructure Using X-ray Computed Tomography, *Soil Sci.*, 2006, **171**(9), 706–718, DOI: 10.1097/01.ss.0000228041.03142.d3.

26 H. Lusic and M. W. Grinstaff, X-ray-Computed Tomography Contrast Agents, *Chem. Rev.*, 2013, **113**(3), 1641–1666, DOI: 10.1021/cr200358s.

27 A. M. Alhammadi, A. AlRatrout, B. Bijeljic and M. J. Blunt, Pore-scale Imaging and Characterization of Hydrocarbon Reservoir Rock Wettability at Subsurface Conditions Using X-ray Microtomography, *J. Visualized Exp.*, 2018, (140), 57915, DOI: 10.3791/57915.

28 A. Scanziani, A. Alhosani, Q. Lin, C. Spurin, G. Garfi, M. J. Blunt and B. Bijeljic, In Situ Characterization of Three-Phase Flow in Mixed-Wet Porous Media Using Synchrotron Imaging, *Water Resour. Res.*, 2020, **56**(9), e2020WR027873, DOI: 10.1029/2020WR027873, acccessed 2023/12/19.

29 A. Alhosani, Q. Lin, A. Scanziani, E. Andrews, K. Zhang, B. Bijeljic and M. J. Blunt, Pore-scale Characterization of Carbon Dioxide Storage at Immiscible and Near-miscible Conditions in Altered-wettability Reservoir Rocks, *Int. J. Greenhouse Gas Control*, 2021, **105**, 103232, DOI: 10.1016/j.ijggc.2020.103232.

30 Y. M. Staedler, D. Masson and J. Schönenberger, Plant Tissues in 3D via X-ray Tomography: Simple Contrasting Methods Allow High Resolution Imaging, *PLoS One*, 2013, **8**(9), e75295, DOI: 10.1371/journal.pone.0075295.

31 S. D. Keyes, N. J. Gostling, J. H. Cheung, T. Roose, I. Sinclair and A. Marchant, The Application of Contrast Media for In Vivo Feature Enhancement in X-ray Computed Tomography of Soil-Grown Plant Roots, *Microsc. Microanal.*, 2017, **23**(3), 538–552, DOI: 10.1017/s1431927617000319.

32 Z. Wang, P. Verboven and B. Nicolai, Contrast-Enhanced 3D Micro-CT of Plant Tissues Using Different Impregnation Techniques, *Plant Methods*, 2017, **13**(1), 105, DOI: 10.1186/s13007-017-0256-5.

33 A. W. J. Heijs, C. J. Ritsema and L. W. Dekker, Three-Dimensional Visualization of Preferential Flow Patterns in Two Soils, *Geoderma*, 1996, **70**(2), 101–116, DOI: 10.1016/0016-7061(95)00076-3.

34 J. Koestel and M. Larsbo, Imaging and Quantification of Preferential Solute Transport in Soil Macropores, *Water Resour. Res.*, 2014, **50**(5), 4357–4378, DOI: 10.1002/2014WR015351.

35 D. Luo, X. Wang, C. Burda and J. P. Basilion, Recent Development of Gold Nanoparticles as Contrast Agents for Cancer Diagnosis, *Cancers*, 2021, **13**(8), 1825, DOI: 10.3390/cancers13081825.

36 J. Turkevich, P. C. Stevenson and J. Hillier, A Study of the Nucleation and Growth Processes in the Synthesis of Colloidal Gold, *Discuss. Faraday Soc.*, 1951, **11**, 55–75, DOI: 10.1039/DF9511100055.

37 C. P. Scotson, M. Munoz-Hernando, S. J. Duncan, S. A. Ruiz, S. D. Keyes, A. van Veelen, I. E. Dunlop and T. Roose, Stabilizing Gold Nanoparticles for Use in X-ray Computed Tomography Imaging of Soil Systems, *R. Soc. Open Sci.*, 2019, **6**(10), 190769, DOI: 10.1098/rsos.190769.

38 A. P. Constantinou, U. Marie-Sainte, L. Peng, D. R. Carroll, C. M. McGilvery, I. E. Dunlop and T. K. Georgiou, Effect of Block Copolymer Architecture and Composition on Gold Nanoparticle Fabrication, *Polym. Chem.*, 2019, **10**(34), 4637–4642, DOI: 10.1039/C9PY00931K.

39 I. E. Dunlop, M. P. Ryan, A. E. Goode, C. Schuster, N. J. Terrill and J. V. M. Weaver, Direct Synthesis of PEG-Encapsulated Gold Nanoparticles Using Branched Copolymer Nanoreactors, *RSC Adv.*, 2014, **4**(53), 27702–27707, DOI: 10.1039/C4RA03500C.

40 P. Zheng, X. Jiang, X. Zhang, W. Zhang and L. Shi, Formation of Gold@Polymer Core–Shell Particles and Gold Particle Clusters on a Template of Thermoresponsive and pH-Responsive Coordination Triblock Copolymer, *Langmuir*, 2006, **22**(22), 9393–9396, DOI: 10.1021/la0609064.

41 E. Seo, S.-H. Lee, S. Lee, S.-H. Choi, C. J. Hawker and B.-S. Kim, Highly Stable Au Nanoparticles with Double Hydrophilic Block Copolymer Templates: Correlation Between Structure and Stability, *Polym. Chem.*, 2017, **8**(31), 4528–4537, DOI: 10.1039/C7PY00773F.

42 N. P. Truong, G. R. Jones, K. G. E. Bradford, D. Konkolewicz and A. Anastasaki, A Comparison of RAFT and ATRP Methods for Controlled Radical Polymerization, *Nat. Rev. Chem.*, 2021, **5**(12), 859–869, DOI: 10.1038/s41570-021-00328-8.

43 M. Rikkou-Kalourkoti, O. W. Webster and C. S. Patrickios, Group Transfer Polymerization, *Encycl. Polym. Sci. Technol.*, 2013, **7**, 580–588, DOI: 10.1002/0471440264.pst603.

44 D. R. Carroll, A. P. Constantinou, N. Stingelin and T. K. Georgiou, Scalable Syntheses of Well-Defined Pentadecablock Bipolymer and Quintopolymer, *Polym. Chem.*, 2018, **9**(25), 3450–3454, DOI: 10.1039/C8PY00565F.

45 M. A. Ward and T. K. Georgiou, Thermoresponsive Triblock Copolymers Based on Methacrylate Monomers: Effect of Molecular Weight and Composition, *Soft Matter*, 2012, **8**(9), 2737–2745, DOI: 10.1039/C2SM06743A.

46 N. Ghasdian, M. A. Ward and T. K. Georgiou, Well-Defined "Clickable" Copolymers Prepared via One-Pot Synthesis, *Chem. Commun.*, 2014, **50**(54), 7114–7116, DOI: 10.1039/C4CC02660H.

© 2025 The Author(s). Published by the Royal Society of Chemistry

RSC Appl. Polym., 2025, **3**, 1596–1612 | 1611

47 G. Cornelis, B. Ryan, M. J. McLaughlin, J. K. Kirby, D. Beak and D. Chittleborough, Solubility and Batch Retention of CeO$_2$ Nanoparticles in Soils, *Environ. Sci. Technol.*, 2011, **45**(7), 2777–2782, DOI: 10.1021/es103769k.

48 J. Klein, Evidence for Reptation in an Entangled Polymer Melt, *Nature*, 1978, **271**(5641), 143–145, DOI: 10.1038/271143a0.

49 J. Crank, *The Mathematics of Diffusion*, Oxford University Press, 1979.

50 S. A. Barber, *Soil Nutrient Bioavailability: a Mechanistic Approach*, John Wiley & Sons, 1995.

51 W. J. Brittain and I. B. Dicker, Termination in Group-Transfer Polymerization, *Macromolecules*, 1989, **22**(3), 1054–1057, DOI: 10.1021/ma00193a010.

52 J. Liu and Y. Lu, Accelerated Color Change of Gold Nanoparticles Assembled by DNAzymes for Simple and Fast Colorimetric Pb2+ Detection, *J. Am. Chem. Soc.*, 2004, **126**(39), 12298–12305, DOI: 10.1021/ja046628h.